Journal of Dynamics, Monitoring and Diagnostics, 2023, 2, 228-242
https://doi.org/10.37965/jdmd.2023.314

ISTP
RESEARCH ARTICLE

An Inter-Shaft Bearing Fault Diagnosis Dataset from an Aero-Engine System

Lei Hou,[1] Haiming Yi,[1] Yuhong Jin,[1] Min Gui,[2] Lianzheng Sui,[2] Jianwei Zhang,[2] and Yushu Chen[1]

[1]School of Astronautics, Harbin Institute of Technology, Harbin 150001, China
[2]Factory of Xiangyang Hangtai Power Machinery, Xiangyang 441000, China

(Received 12 May 2023; Revised 19 June 2023; Accepted 02 August 2023; Published online 03 August 2023)

Abstract: In this paper, the aero-engine test with inter-shaft bearing fault is carried out, and a dataset is proposed for the first time based on the vibration signal of rotors and casings. First, a test rig based on a real aero-engine is established, driven by motors and equipped with a lubricating system. Then, the aero-engine is disassembled and assembled following the specification process, and the inter-shaft bearing with artificial fault is replaced. Next, the aero-engine test is conducted at 28 groups of high- and low-pressure speeds. Six measuring points are arranged, including two displacement sensors to test the displacement vibration signals of the low-pressure rotor and four acceleration sensors to test the acceleration vibration signals of the casing. The test results are integrated into an inter-shaft bearing fault dataset. Finally, based on the dataset in this paper, frequency spectrum, envelope spectrum, CNN, LSTM, and TST are used for fault diagnosis, and the results are compared with those of CWRU and XJTU datasets. The results show that the characteristic fault frequency cannot be found directly in the spectrum and envelope spectrum corresponding to this paper's dataset but in CWRU and XJTU datasets. Using CNN, LSTM, and TST for fault diagnosis of the dataset in this paper, the accuracy is 83.13%, 85.41%, and 71.07%, respectively, much lower than the diagnosis results of CWRU and XJTU datasets. It can be seen that the dataset in this paper is closer to the actual fault diagnosis situation and is a more challenging dataset. This dataset provides a new benchmark for the validation of fault diagnosis methods. Mendeley data: https://github.com/HouLeiHIT/HIT-dataset.

Keywords: aero-engine test; dataset; fault diagnosis; inter-shaft bearing

I. INTRODUCTION

Aero-engine is the core component of an aircraft, and its stable operation guarantees the safe flight of the aircraft. In a dual-rotor aero-engine, the aircraft rolling bearing is a crucial load-bearing component, and the operating environment is harsh and highly prone to failure, causing severe accidents. Therefore, establishing aircraft rolling bearing fault datasets and conducting research on aero-engine fault diagnosis can help to timely identify the early minor fault characteristics of aircraft rolling bearings and avoid accidents [1–3].

In existing research, the fault diagnosis of aircraft rolling bearings is mainly conducted through bearing vibration signals. Hou *et al.* [4] proposed a feature extraction technique for inter-shaft bearing faults under noisy conditions, using Laplace wavelet and orthogonal matching pursuit algorithm combined with sparse representation theory. The method effectively extracted weak-bearing fault features by identifying the transient shock component. Yang *et al.* [5] focused on high-speed rotor systems and established a symmetrical rigid bearing-rotor model. They took the envelope analysis to research the dynamic response and qualitatively verified the response by the experimental results. Wang *et al.* [6] proposed an inter-shaft bearing fault diagnosis method called Improved Spiking Neural Network (ISNN), and the ISNN was superior to the previous Spiking Neural Network (SNN). Yu *et al.* [7] proposed an algorithm that combines information fusion, wavelet transform (WT), singular value decomposition (SVD), Katz fractal dimension, and Cross-Correlation Function (CCF), called CCF-WT-SVD-Katz. Each part of the algorithm could achieve signal denoising, enhance reconstruction, and extract fault features. Liu *et al.* [8] developed a combined model of LSTM network with deep CNN and conducted theoretical and experimental research. The results showed that the prediction accuracy of the method reached 99.94% and 98.67%, which was better than the single deep CNN and LSTM. Liu *et al.* [9] proposed a combined method of deep learning and particle filter. The validity of the method was verified by whole lifetime test of bearings, and the results showed that this method got a prediction accuracy of 2.19%, 0.93%, and 1.43% higher than RMS values. Zhang *et al.* [10] developed a blind extraction method for multi-channel fault signals based on the CCA criterion, which took the bearing fault frequency to calculate the delay parameter. The simulation and experimental results demonstrated that this method had better accuracy and convergence speed. Hou *et al.* [11] developed a Siamese Multiscale Residual Feature Fusion Network (SMSRFFN) for small-sample conditions of aero-engine bearing fault diagnosis. Conducting tests by existing datasets and the results demonstrated the validity of the SMSRFFN in fault diagnosis accuracy under minor sample conditions. Pan *et al.* [12] proposed a combination of Intrinsic Time-scale Decomposition (ITD) and Singular Value Decomposition (SVD) to diagnose compound bearing faults. Compared with ITD and PCA methods,

Corresponding author: Lei Hou (e-mail: houlei@hit.edu.cn).

the results showed that the ITD-SVD method gets a higher accuracy under noise. Wang *et al.* [13] developed a planetary gearbox fault diagnosis method by conducting a transferable deep Q network (TDQN). The test results showed that the TDQN got an accuracy of 98.53% in a source task, 99.63% and 98.37% in two target tasks.

Datasets are crucial in verifying the effectiveness of fault diagnosis methods, and the common fault diagnosis datasets include Case Western Reserve University (CWRU) dataset [14] and Xi'an Jiaotong University (XJTU) dataset [15]. These datasets provide data support for the validation of bearing fault diagnosis methods. However, these datasets have a single research object and are mainly focused on bearing vibration signals, which cannot meet the fault diagnosis needs of other machines. Therefore, some researchers established new datasets based on different machines. Kumar *et al.* [16] took vibration analysis for motor bearing fault detection using triaxial vibration data acquired with a MEMS-based accelerometer and NI myRIO and established a motor bearing fault dataset. The dataset included healthy and faulty bearing conditions under different loads and was useful for assessing new fault diagnosis methods. Jung *et al.* [17] established a time series dataset based on rotating machines' temperature, vibration, driving current, and acoustic data. The rotating machine conditions included normal, shaft misalignment, bearing faults, and rotor unbalance. The dataset could be used to verify methods for rotating machines' fault diagnosis. Lessmeier *et al.* [18] presented a benchmark dataset of rolling bearings with damage, which used the motor current signal of an electromechanical drive system as data. The dataset included damage in external bearings with a wide distribution of bearing damage. The classification accuracy was lower compared to classifications based on vibration signals, which meant it could be used for further research. In addition, the image-based bearing fault diagnosis [19], helpful motor life estimation [20–22], bearing life prediction [15,23–26], and gear fault diagnosis [27] also had corresponding datasets for research. It can be seen that the corresponding dataset is crucial in the field of fault diagnosis, health monitoring, and anomaly detection of rotating machinery.

To sum up, in the existing research on machine learning methods for aircraft rolling bearing fault diagnosis of an aero-engine, the training and testing set is based on the publicly released datasets of the bearing fault. Replacing inter-shaft bearings is complicated and difficult, so there are no publicly released datasets about the aircraft rolling bearing fault data based on the aero-engine signals of the rotors and casings. In this paper, we build a test rig, take the aero-engine tests with inter-shaft bearing faults, and establish a dataset based on the result of the tests. The main contributions of this paper are listed as follows.

(1) An inter-shaft bearing fault dataset is released for the first time based on the aero-engine system, which comes from the vibration response of the aero-engine rotor and casings rather than just from bearing test bench data. The released dataset is closer to the aero-engines actual excitation state and vibration coupling.

(2) The dataset includes three types of data: healthy, inner ring fault, and outer ring fault. The rotor speed range ranges from 1000 r/min to 6000 r/min. The measurement points are arranged on the rotor and casings, and the vibration signals include displacement and acceleration signals.

(3) The paper applies frequency spectrum, envelope spectrum, CNN, LSTM, and TST methods for preliminary dataset analysis and finds that the dataset can be diagnosed using existing fault diagnosis methods, which indicates universality. Comparing the diagnosis results with those of the XJTU and CWRU datasets, it is found that the fault diagnosis of the dataset in this paper is more complicated, which provides a challenging new benchmark for performance evaluation of subsequent fault diagnosis methods.

The rest of this paper is arranged as follows. In Section II, the structure of the test rig is described. In Section III, the procedure of the test was introduced. Section IV establishes the dataset and does inter-shaft bearing fault diagnosis analysis based on it. Section V summarizes the conclusions of this paper.

II. AERO-ENGINE TESTS

A. TEST RIG OF AERO-ENGINE

Vibration analysis of aero-engines plays a critical role in ensuring their safety and reliability during operation. To accurately obtain the vibration response of an aero-engine and simulate the inter-shaft bearing faults, a test rig that replicates the real-life operating conditions is essential. In this study, we established a test rig based on a real aero-engine to measure the vibration response of the engine during operation. The test rig comprises three main components: a modified aero-engine, a motor drive system, and a lubricant system. The modified aero-engine serves as the core component of the test rig and is responsible for generating the vibration signals during operation. The motor drive system, on the other hand, provides the necessary driving force to run the aero-engine at different speeds and loads, while the lubricant system ensures that the engine runs smoothly and efficiently. The physical map of the test rig is shown in Fig. 1.

The modified aero-engine utilized in the test rig involves the removal of the rotor blades, combustion chamber, and certain accessory casings. And the crucial dual-rotor structure, which constitutes the main component of the aero-engine, is preserved. This dual-rotor structure includes both the low-pressure (LP) compressor and high-pressure (HP) compressor and the LP turbine and HP turbine. The main load-bearing casing, inter-shaft bearing, and five

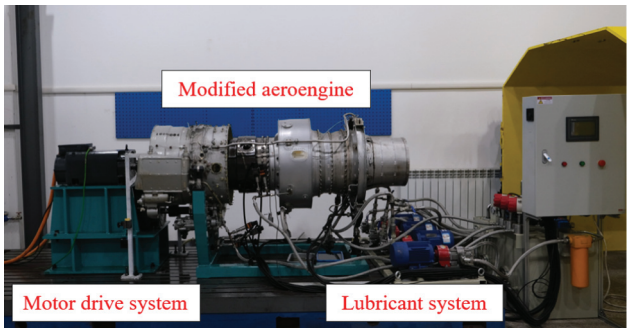

Fig. 1. The test rig based on a real aero-engine.

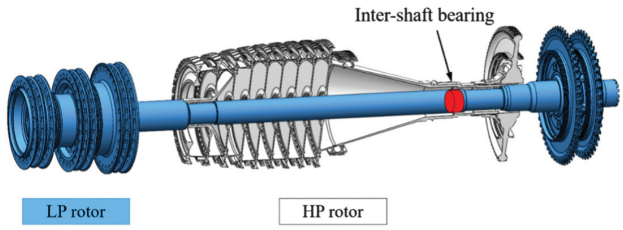

Fig. 2. Three-dimensional model of dual-rotor structure.

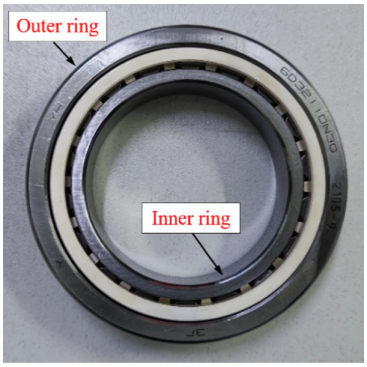

Fig. 3. The inter-shaft bearing.

support bearings are also preserved. The dual-rotor structure is depicted in Fig. 2, while the inter-shaft bearing is displayed in Fig. 3. Table I provides the pertinent parameter information.

In the motor drive system, two motors are utilized in the test rig to drive the LP rotor and HP rotor. The LP motor directly drives the LP rotor, while the HP motor drives the HP rotor through a speed-raising gearbox. Figure 4 depicts the motors employed in the test rig, and Table II presents the parameter information of the motors, including the rated current, rated moment, and rated speed. The motors play a crucial role in the test rig, as they drive the rotors and generate the vibration responses. Therefore, selecting suitable motors with appropriate parameters is essential to guarantee the accuracy and reliability of the test results. Based on the requirements of the test rig, the LP motor and HP motor were chosen carefully, ensuring that they meet the necessary specifications for the test rig.

A lubricant system is equipped on the test rig for lubricating and cooling effects. It includes three oil-feed pumps, an oil scavenger pump, and a heat pump prepared with temperature sensors, which enable the system to realize the function of temperature control and maintain

Table I. Parameter information of inter-shaft bearing

Parameter	Value
Number of rolling elements	15pc.
Diameter of inner ring	30 mm
Diameter of outer ring	65 mm
Diameter of pitch circle	55 mm
Rolling element diameter	7.5 mm
Nominal pressure angle	0°N

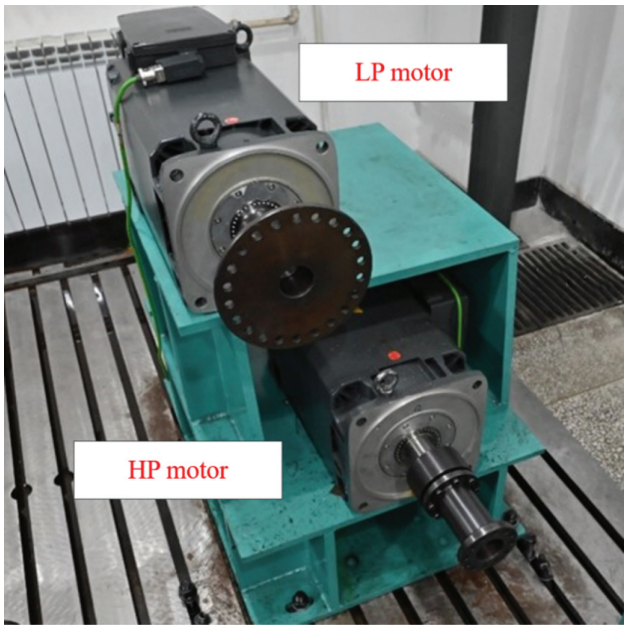

Fig. 4. The LP motor and HP motor.

Table II. Information of LP and HP motors

Name	Manufacturer	Model number	Parameter	Value
LP motor	SIEMENS	1PH8137-1SG03	I_{max}	152A
			M_{max}	340 Nm
			n_{max}	10,000 rpm
HP motor	SIEMENS	1PH8137-1SS03	I_{max}	130A
			M_{max}	320 Nm
			n_{max}	15,000 rpm

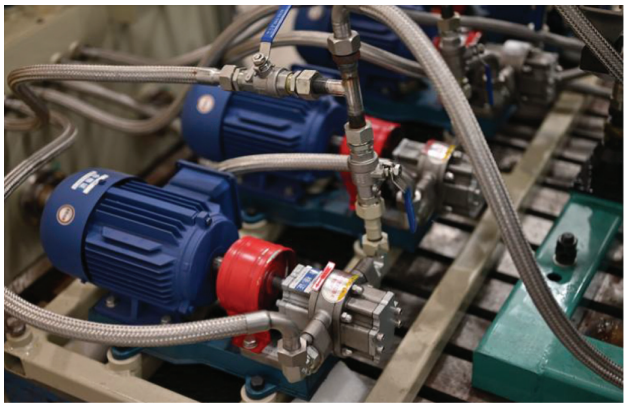

Fig. 5. The oil-feed pumps.

a stable temperature for optimal performance. The oil-feed pumps are shown in Fig. 5.

In addition, to ensure the safety of testers and equipment, three metal protective covers are installed to prevent any accidents caused by falling parts. The monitoring system is also set up to detect any potential anomalies in real time, enabling prompt actions. The protective metal

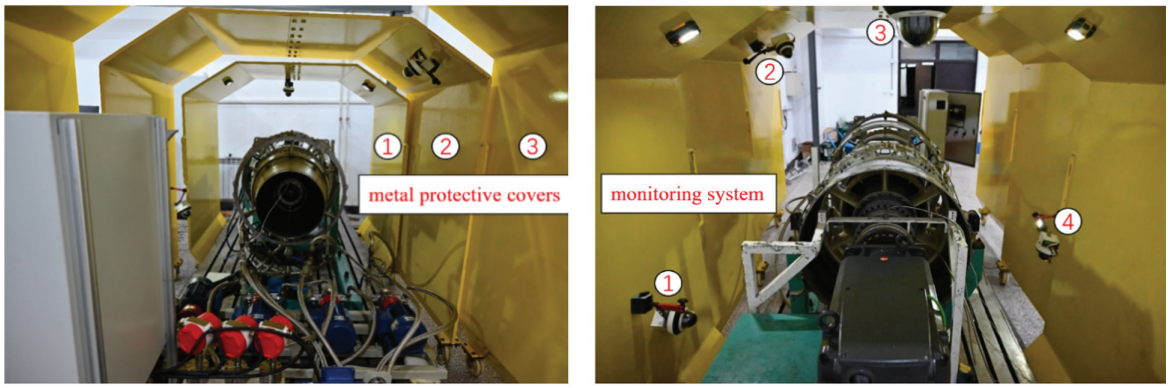

(a) (b)

Fig. 6. (a) Metal protective covers. (b) Monitoring system.

covers and monitoring system can be observed in detail in Fig. 6, providing a comprehensive overview of the safety measures in place for the test rig.

B. ARTIFICIAL FAULTS OF INTER-SHAFT BEARING

The study of bearing fault diagnosis often involves creating artificial faults and conducting simulation tests to obtain fault characteristics. This approach can also be applied to the inter-shaft bearing fault diagnosis of aero-engines. Artificial faults, such as those found in the inner and outer rings, can cause periodic shocks on the rolling balls during rotation. These periodic shock signals are similar to those caused by actual faults, making them an effective tool for diagnosing faults.

This study sequentially fitted three inter-shaft bearings with artificial faults into the modified aero-engine. These included one bearing with an outer ring fault and two with inner ring faults. The artificial faults were created by wire cutting, as shown in Fig. 7, and the relevant bearing information and fault dimensions are listed in Table III.

Table III. Fault information of inter-shaft bearings with artificial fault

No.	Fault position	Depth of fault/mm	Length of fault/mm
1	Outer ring	0.5	0.5
2	Inner ring	0.5	0.5
3	Inner ring	0.5	1.0

III. PREPARATION OF TEST

To obtain the vibration characteristic of the aero-engine under fault conditions, the inter-shaft bearing needs to be replaced by those with artificial faults in Section 2.B. The complex structure of an aero-engine makes it difficult to disassemble and assemble; therefore, there is almost no research involved in the replacement of inter-shaft bearings of an aero-engine in the existing research. In this paper, testers disassemble the aero-engine, replace the inter-shaft bearing, assemble the aero-engine, and install the aero-engine on the test rig under the guidance of professional engineers. A custom-made assembly wagon holds the aero-engine in place during the disassembly and assembly process. After replacing the inter-shaft bearing and assembling the aero-engine, the aero-engine can be installed on the test rig and connected to the motor drive and lubricant systems. The specific steps of the disassembly and assembly process are shown as follows.

A. PREPARATORY WORK

It is necessary to ensure the power and oil are off before the disassembly begins. And then, the aero-engine needs to be separated from the motor drive and lubricant systems. The

(a) (b) (c)

Fig. 7. The inter-shaft bearings with artificial (a) outer ring fault, (b) inner ring fault, (c) inner ring fault.

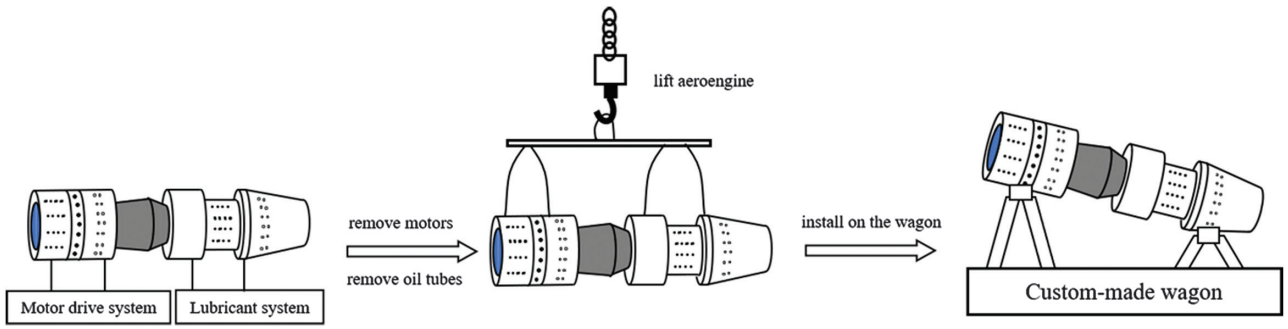

Fig. 8. The schematic diagram of preparatory work.

aero-engine is connected to the motors by couplings and wire and with a lubricant system by oil pipes. After secession, the crane is used to lift the aero-engine and install it on the custom-made assembly wagon. The process of preparatory work is shown in Fig. 8.

B. DISASSEMBLE AERO-ENGINE

It's a complex process to disassemble the aero-engine, and many customized tools and wagons are used in the disassembly process. The disassembly process can be roughly divided into four steps.

Step 1, the support and transmission components are disassembled in sequence, including the fan casing, transfer gearbox, main transmission casing, central driving shaft, and tail casing, as shown in Fig. 9.

Step 2, the components related to the LP turbine disassembled, such as LP compressor disks, LP turbine disks, LP turbine shaft, and LP turbine blades, as shown in Fig. 10.

Step 3, the HP turbine components are disassembled, such as HP turbine disk, HP turbine shafts, and HP turbine blade, as shown in Fig. 11.

Step 4, the HP casing and the combustor casing are disassembled, and then, the crane can lift the HP rotor. The inter-shaft bearing remains in a tubular structure called a combustion cylinder. To remove it, the tubular structure needs to be heated to 205°C, and customized tools can

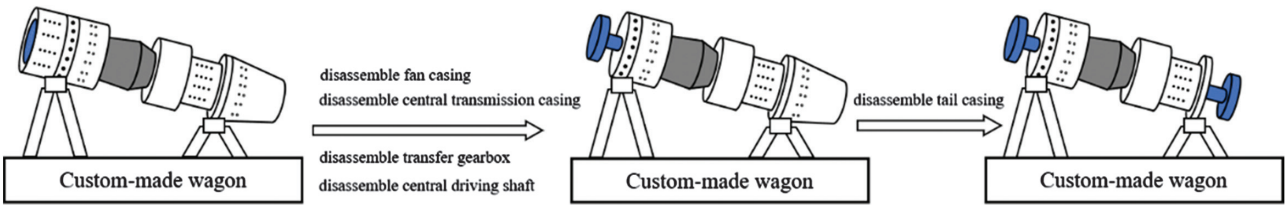

Fig. 9. The schematic diagram of step 1.

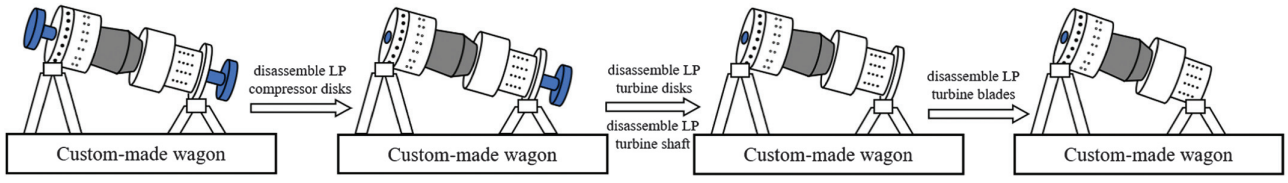

Fig. 10. The schematic diagram of step 2.

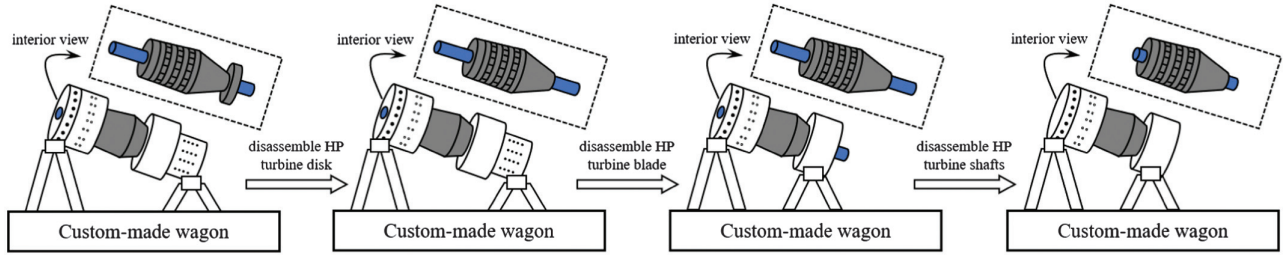

Fig. 11. The schematic diagram of step 3.

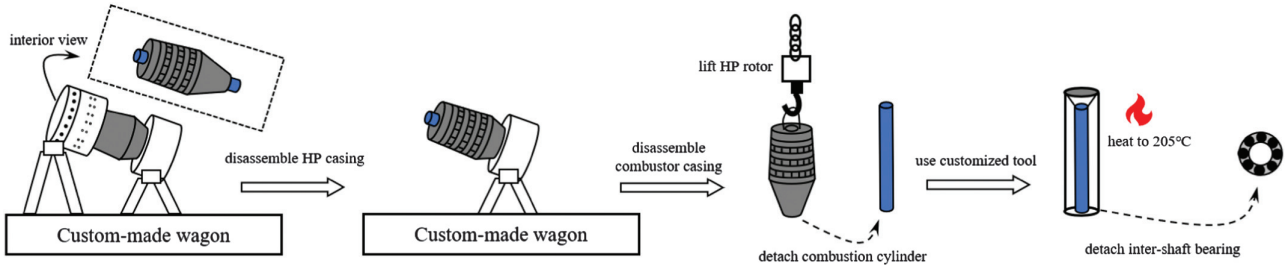

Fig. 12. The schematic diagram of step 4.

detach the inter-shaft bearing. The primary process is shown in Fig. 12.

C. ASSEMBLE AERO-ENGINE

The assembly process is the reverse process of disassembly. After replacing the inter-shaft bearing to be tested, the components are assembled following steps 4 through 1 in section 2.3.2. After assembling the aero-engine and installing it on the test rig, the motor drive system and the lubricant system need to be connected to the aero-engine; then, the test rig is ready for the test.

D. TEST OF AERO-ENGINE WITH INTER-SHAFT BEARING FAULT

The arrangement of testing points is shown in Fig. 13. Two eddy current sensors are used to measure the horizontal and vertical vibration displacement response of the LP rotor. Four acceleration sensors are used to measure the normal vibration acceleration response of the casings, and the information of the sensors is shown in Table IV. The number of testing points corresponds to the channel number in the dataset.

After ensuring the regular operation of the test rig and the correct arrangement of measuring points, the test can proceed as planned. The displacement and acceleration

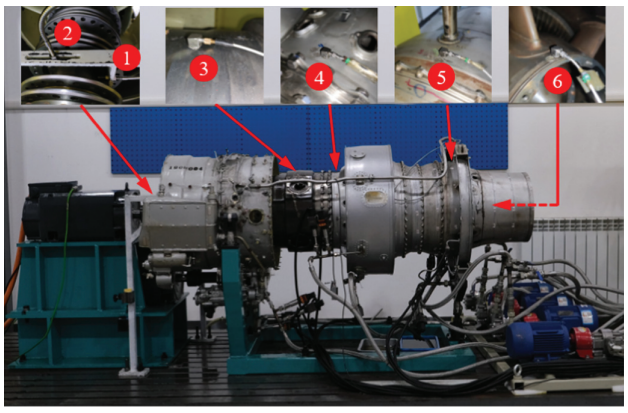

Fig. 13. The arrangement of testing points.

Table IV. Information of sensors

Sensor type	Sensor model	Measure point
Displacement	KISTLER 8776A50M1	1, 2
Acceleration	K9000XL	3, 4, 5, 6

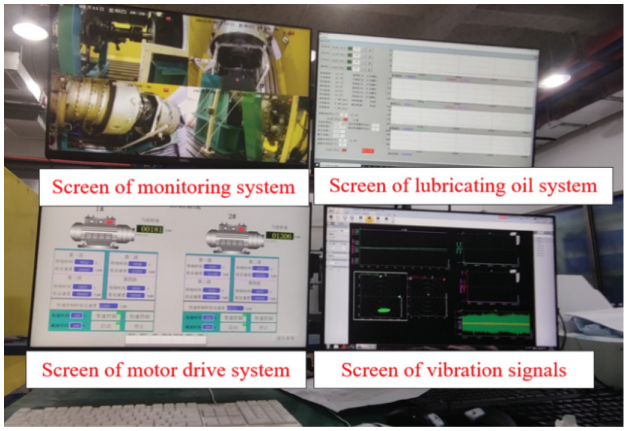

Fig. 14. The monitoring screen of the test.

sensors collect signals and input them through the TRION-2402-dACC differential multifunctional module. These signals are analyzed by the DEWETRON DEWE2-M7 and saved on the computer for later analysis. The sampling frequency is set to 25,000 Hz. The testers control and monitor the test via computer, and the real-time test status is displayed on screens, as shown in Fig. 14. The test plan for rotor speed is presented in Table V. During the test, the signals recorded by the sensors are stored in the computer while both HP and LP rotors accelerate to the designated speed. For each bearing, a total of 28 data groups should be collected before the aero-engine is disassembled to replace the next bearing under test.

IV. DATASETS AND BENCHMARK STUDY

A. DATASETS OF AERO-ENGINE WITH INTER-SHAFT BEARING FAULT

The test is carried out five times and five datasets of three states of inter-shaft bearings are obtained, which are stored in the form of a time series. Each dataset is stored as a three-dimensional array, such as $[A]_{a\times b\times c}$. Raw data are a long time series of 15 seconds of sampling. The sampling frequency is 25,000 Hz. The raw data are segmented and truncated for subsequent analysis into a short time series containing 20,480 data points. After eliminating invalid data, 2412 sets of data are retained in the datasets in total.

For each dataset, each row corresponds to the same test, the first two columns store the displacement response, and

Table V. The test plan for rotor speed

LP speed (r/min)	HP speed (r/min)	Speed ratio	LP speed (r/min)	HP speed (r/min)	Speed ratio
1000	1200	1.2	4400	5280	1.2
1500	1800	1.2	4500	5400	1.2
2000	2400	1.2	4600	5520	1.2
2500	3000	1.2	4700	5640	1.2
3000	3600	1.2	4800	5760	1.2
3500	4200	1.2	4900	5880	1.2
3600	4320	1.2	5000	6000	1.2
3700	4440	1.2	3000	3600	1.2
3800	4560	1.2	3000	3900	1.3
3900	4680	1.2	3000	4200	1.4
4000	4800	1.2	3000	4500	1.5
4100	4920	1.2	3000	4800	1.6
4200	5040	1.2	3000	5100	1.7
4300	5160	1.2	3000	5400	1.8

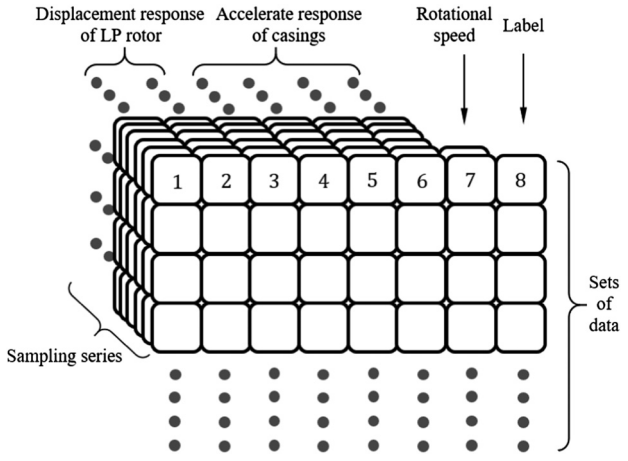

Fig. 15. The schematic diagram of the datasets.

columns 3 through 6 store the acceleration response. Column 7 stores the high- and low-speed information of this test. In the datasets, the states of inter-shaft bearings are distinguished by labels, that label '0' represents 'health inter-shaft bearing', label '1' means 'inter-shaft bearing with inner ring fault', and label '2' represents 'inter-shaft bearing with outer ring fault'. The label information is stored at column 8. The schematic diagram of the datasets is shown in Fig. 15, and the essential information of the datasets is shown in Table VI.

B. BENCHMARK STUDY OF SPECTRUM ANALYSIS

In the research of bearing fault diagnosis, frequency spectrum analysis is a common method. The characteristic frequency peaks on the frequency spectrum can be used to determine whether a fault occurs. As for the original vibration signals with excessive noise components, the envelope signal can be obtained by the envelope transformation of the original signal to reduce the interference of noise components. In order to compare the dataset in this paper with the CWRU and XJTU datasets, a group of signals with bearing inner ring fault is taken as an example, the information of these dataset signals is shown in Table VII. The acceleration time histories of three datasets are shown in Fig. 16, and the frequency spectrums are shown in Fig. 17.

Table VI. Information of the datasets.

Name	Fault position	Depth of fault/mm	Length of fault/mm	Sampling frequency/Hz	LP and HP speed(r/min)	Length per series	Number of series
data1	none	0	0	25000	LP speed range:	20480	504×6
data2	none	0	0	25000	1000~5000	20480	450×6
data3	inner ring	0.5	0.5	25000	HP speed range:	20480	504×6
data4	inner ring	0.5	1.0	25000	1200~6000	20480	504×6
data5	outer ring	0.5	0.5	25000		20480	450×6

Table VII. Information of the compared signals

Datasets	Fault position	Fault type	Size of fault	Sampling frequency	Motor speed/rpm	Signal type
Proposed	inner ring	Artificial	0.5	25000 Hz	2000/2400	Acceleration
CWRU	inner ring	Artificial	0.5334	12000 Hz	1797	Acceleration
XJTU	inner ring	Run-to-failure	None	25600 Hz	2250	Acceleration

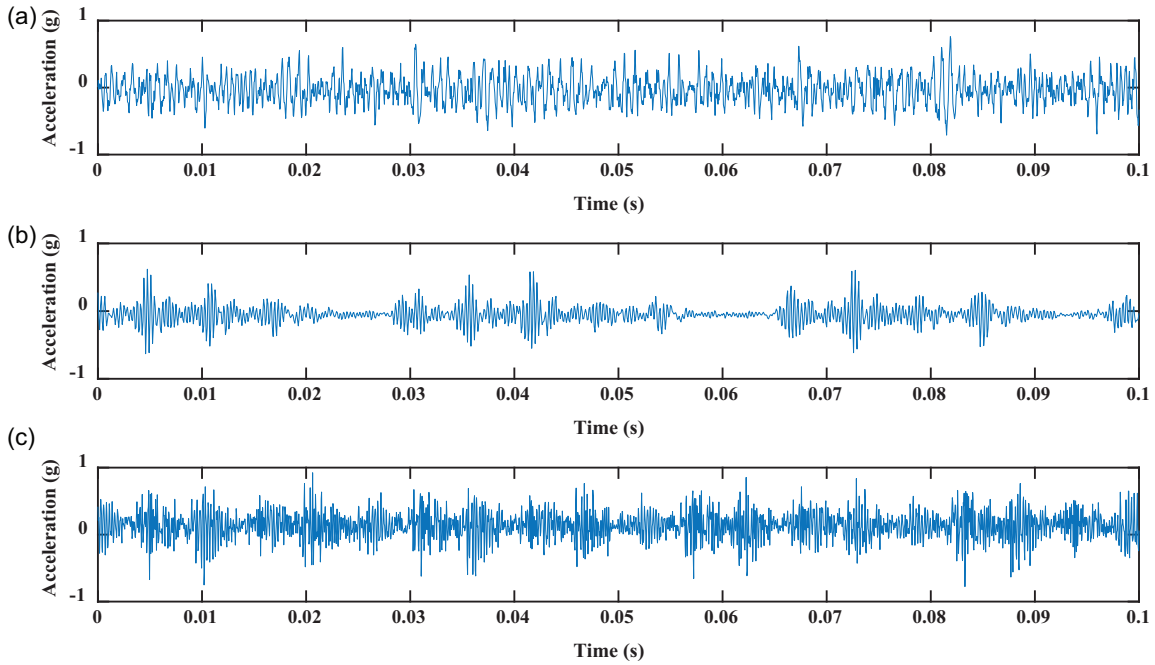

Fig. 16. The time histories of bearing with inner ring fault. (a) Dataset of this paper. (b) CWRU dataset. (c) XJTU dataset.

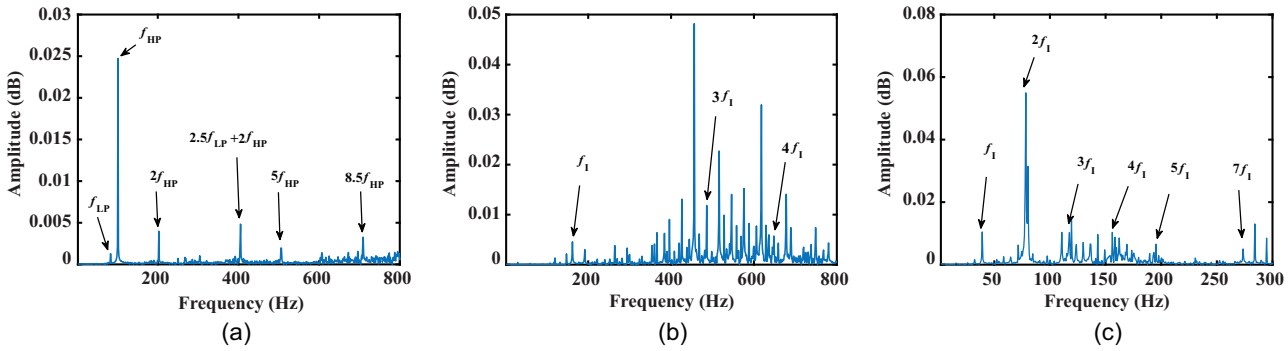

Fig. 17. The frequency spectrums of bearing with inner ring fault. (a) Dataset of this paper. (b) CWRU dataset. (c) XJTU dataset.

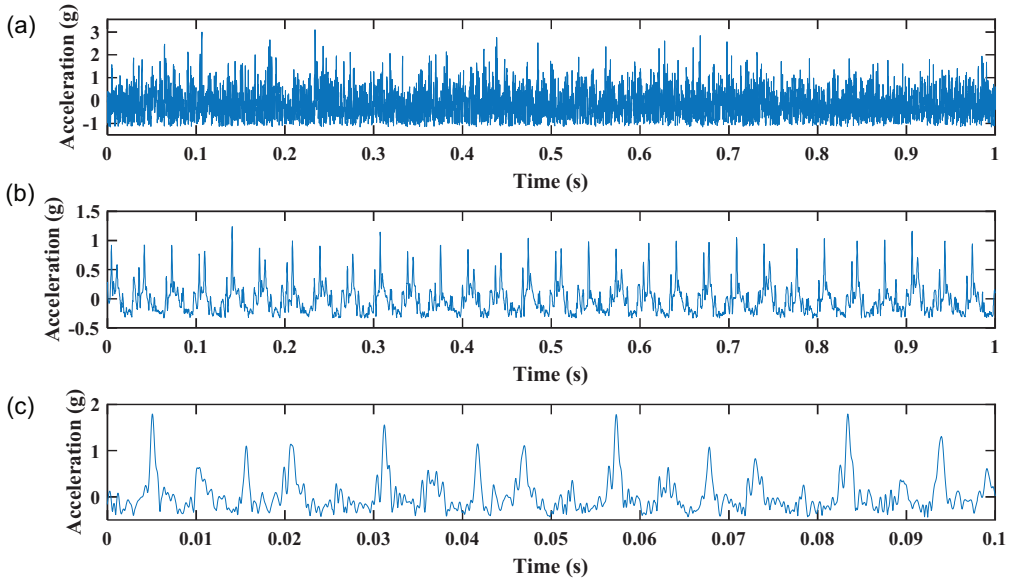

Fig. 18. The envelope signals of bearing with inner ring fault. (a) Dataset of this paper. (b) CWRU dataset. (c) XJTU dataset.

The acceleration time histories in Fig. 16 show that the vibration signal of this paper is closer to a random signal, while the signals of CWRU and XJTU exhibit a more pronounced impact phenomenon. From the frequency spectrums shown in Fig. 17, it can be seen that there are lots of frequency components that appear in the frequency spectrums. In the frequency spectrum of the dataset of this paper in Fig. 17(a), the main frequency components are the frequency f_{HP} and its doubling frequencies $2f_{HP}$, $5f_{HP}$ and so on. The combined frequency $2.5f_{LP}+2f_{HP}$ also corresponds to a frequency peak. But the inner fault characteristic frequency f_I can't be found in the frequency spectrum, so it's hard to fault diagnosis directly by frequency spectrum. While in the frequency spectrum of CWRU in Fig. 17(b), the inner ring fault characteristic frequency f_I and its doubling frequencies $3f_I$ and $4f_I$ can be found and in the frequency spectrum of XJTU in Fig. 17(c), the inner ring fault characteristic frequency f_I and its doubling frequencies $2f_I$, $3f_I$, $4f_I$, $5f_I$ and $7f_I$ can be found, these noticeable fault features can be directly used for fault diagnosis.

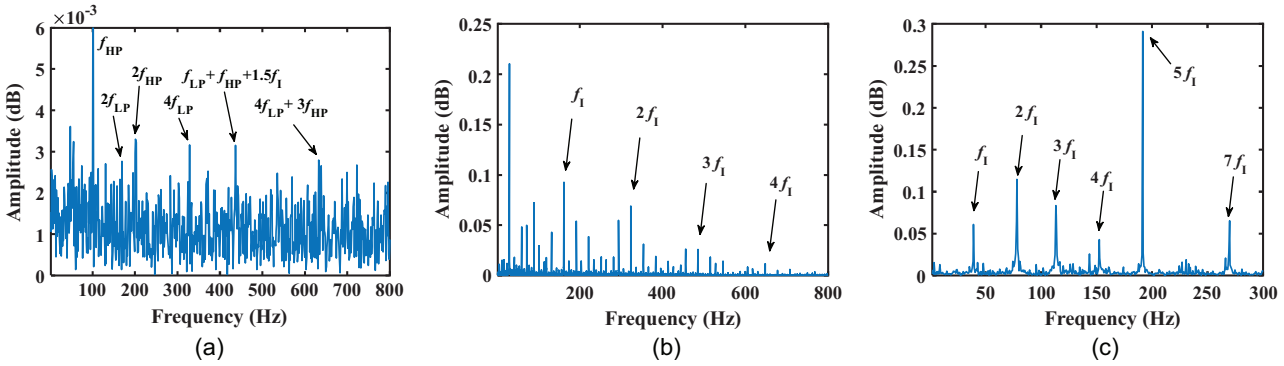

Fig. 19. The envelope spectrums of bearing with inner ring fault. (a) HIT dataset. (b) CWRU dataset. (c) XJTU dataset.

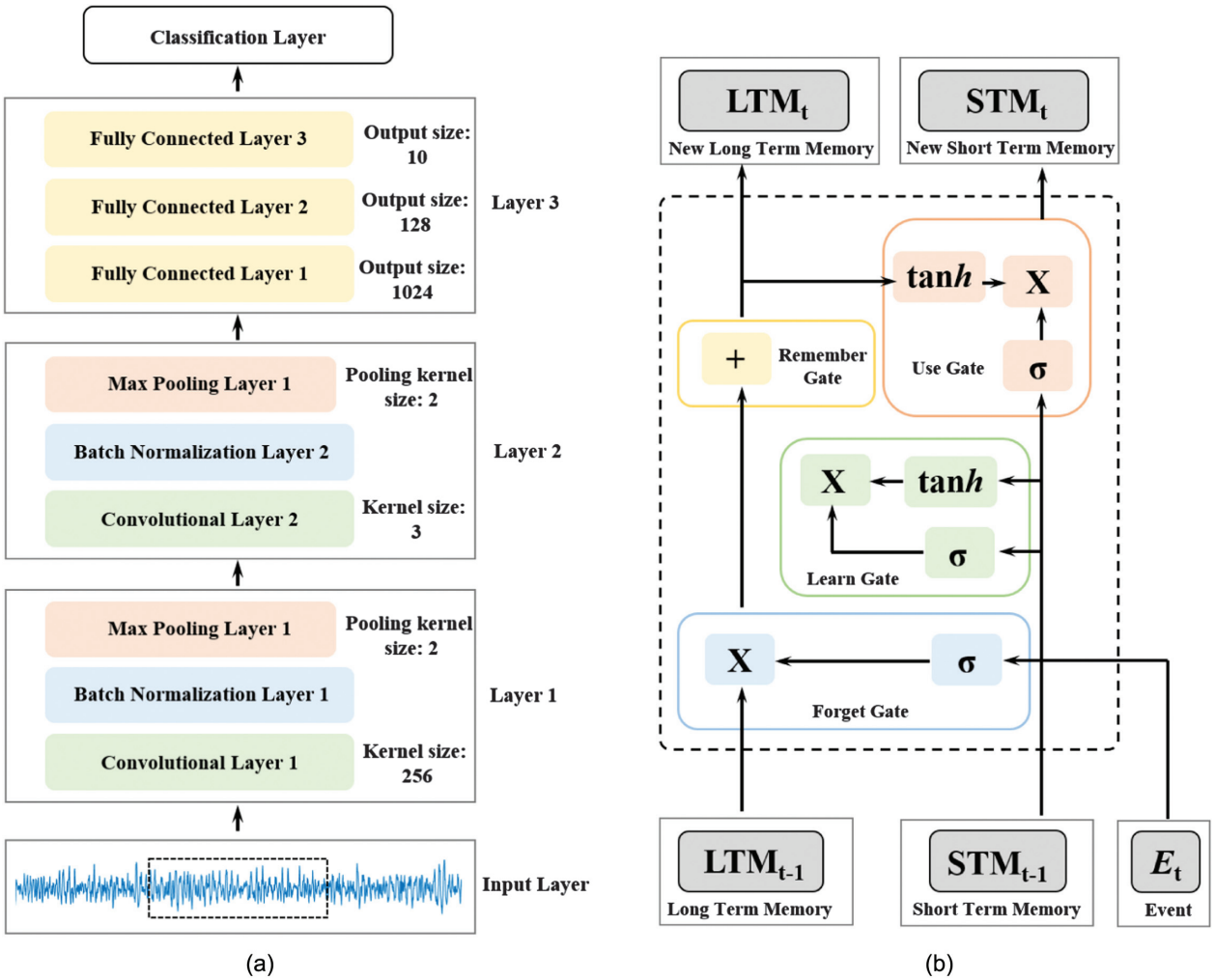

Fig. 20. Structure of (a) CNN model. (b) LSTM model.

In summary, it is impossible to analyze the frequency spectrum of the dataset in this paper for the fault diagnosis. The main reason is that the testing point is arranged on the casing. Therefore, the fault characteristics appear distorted in the transmission process. During the transmission process, the signal of fault character is tapering off and the collisions between connected structures may produce noise, which makes the composition of the vibration signal more complex. In addition, there are also many other frequency components in the frequency spectrum of CWRU and XJTU datasets besides fault features. To reduce the interference of noise signal and amplify the impact effect, the envelope signals obtained by the envelope transformation are shown in Fig. 18 and the envelope spectrums are shown in Fig. 19.

From the envelope signals in Fig. 18, it can be seen that the envelope signals in Fig. 18(a) don't show significant periods, while the signals from the CWRU and XJTU datasets exhibit significant periodicity. In the envelope spectrums of CWRU and XJTU datasets in Fig. 19(b)

Table VIII. The detailed structure of CNN and LSTM models

Model	Structure parameters
CNN	$\begin{bmatrix}\text{Conv1D}(1,25,256)\\ \text{BatchNorm}(25)\\ \text{ReLU}\\ \text{Maxpool1D}(2,2)\end{bmatrix} \rightarrow \begin{bmatrix}\text{Conv1D}(25,50,3)\\ \text{BatchNorm}(50)\\ \text{ReLU}\\ \text{Maxpool1D}(2,2)\end{bmatrix} \rightarrow \begin{bmatrix}\text{Linear}(22350,1024,\text{ReLU})\\ \text{Linear}(1024,128,\text{ReLU})\\ \text{Linear}(128,10)\end{bmatrix}$
LSTM	$\text{Conv1D}(1,128,3) \rightarrow \begin{bmatrix}\text{LSTM}(45,64,\tanh)\\ \text{Dropout}(0.1)\end{bmatrix} \rightarrow \begin{bmatrix}\text{Linear}(64,128,\text{GeLU})\\ \text{Dropout}(0.1)\\ \text{Linear}(128,10,\text{ReLU})\end{bmatrix}$

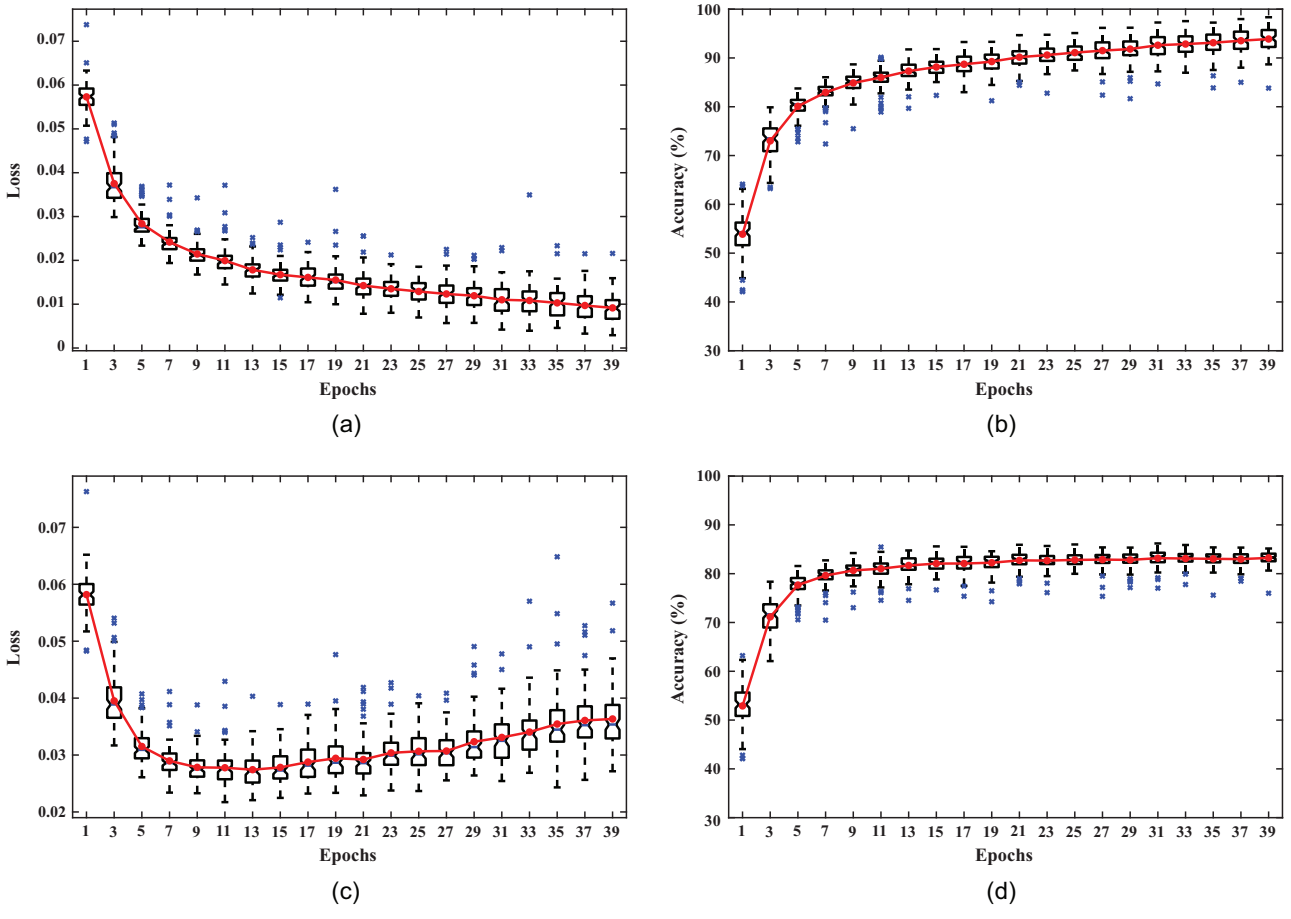

Fig. 21. The fault diagnosis results of CNN. (a) Loss function value of training set. (b) Accuracy of training set. (c) Loss function value of test set. (d) Accuracy of test set.

and Fig. 19(c), the inner ring fault characteristic frequencies are more evident than in frequency spectrums. In the envelope spectrums of the dataset of this paper in Fig. 19(a), the frequency components are more complex, which means the fault characteristics are distorted seriously during the transmission. The envelope spectrums have more combined frequency components, especially those related to f_{LP} and f_{HP}. The fault frequencies appear in Fig. 19(a) as the form of combined frequencies $f_{LP}+f_{HP}+1.5f_I$, but the amplitude of peaks in the envelope spectrums are approximate and the peaks related to the fault frequencies are not the highest. That means the envelope spectrum is hard to be used as the basis for fault diagnosis. The fault characteristics can't be separated by traditional fault diagnosis methods such as spectrum and envelope analysis. This also indicates that the inter-shaft bearing diagnosis based on casing signals is challenging and the datasets of this paper deserve further fault diagnosis study.

C. BENCHMARK STUDY OF MACHINE LEARNING

Based on the datasets collected in this paper, Convolutional Neural Networks (CNN) and Long Short-Term Memory (LSTM) models are utilized for inter-shaft bearing fault diagnosis. CNN is proven to possess a strong ability in feature extraction [8], and LSTM excels at obtaining long-term dependencies [17]. The structures and parameters of CNN and LSTM models are shown in Fig. 20 and Table VIII.

The data from 6 channels are sequenced to generate a two-dimensional time series array for machine learning training and testing. The data were divided into training sets and test sets with 70% and 30% of the data, respectively. The CNN was trained over 40 epochs, while the LSTM was trained over 80 epochs to obtain the fault mode. The accuracy of the models was verified by testing the fault diagnosis on the test set. The boxplot of loss function values and accuracies are shown in Fig. 21 and 22.

Based on the model loss functions and accuracy diagrams of CNN depicted in Fig. 21, it is observed that the loss functions of CNN decrease gradually with an increase in epochs. The test set accuracy of CNN stabilizes at over 80% in just 10 epochs. In Fig. 21(c), the loss function of the test set increases inversely after 30 epochs, after excluding the influence factors such as overfitting, the study found that this may be caused by the structure of CNN or the influence of noise signal in the dataset. That means the fault diagnosis of this dataset deserves further in-depth research. From Fig. 22, it can be found that the loss function of the test set of LSTM decreases gradually with an increase and stabilize in 40 epochs. The test set accuracy of LSTM stabilizes at over 81% in 50 epochs, which converges more slowly but with higher accuracy than CNN. The average loss function values and accuracies of CNN and LSTM are presented in Table IX and X, respectively.

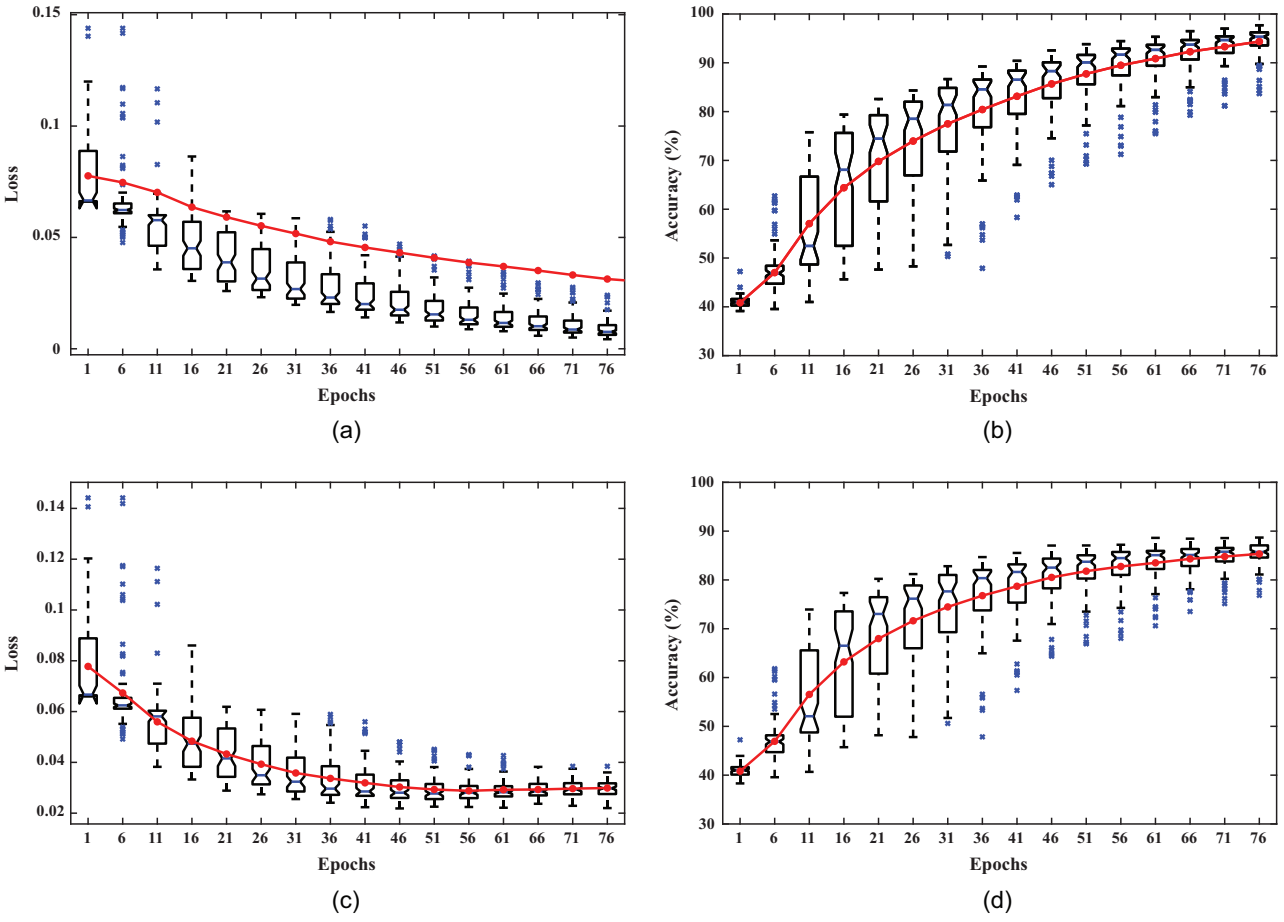

Fig. 22. The fault diagnosis results of LSTM. (a) Loss function value of training set. (b) Accuracy of training set. (c) Loss function value of test set. (d) Accuracy of test set.

Table IX. The average loss function values and accuracies of CNN

Epochs	Average loss function values		Average accuracy	
	Training set	Test set	Training set (%)	Test set (%)
1	0.0573	0.0582	53.89	52.91
5	0.0283	0.0315	80.10	77.67
10	0.0206	0.0277	85.50	80.93
15	0.0167	0.0278	88.14	82.07
20	0.0145	0.0293	89.96	82.71
25	0.0129	0.0307	91.10	82.82
30	0.0117	0.0330	92.00	82.84
35	0.0103	0.0354	93.12	83.04
40	0.0091	0.0376	94.04	83.13

Table X. The average loss function values and accuracies of LSTM

Epochs	Average loss function values		Average accuracy	
	Training set	Test set	Training set (%)	Test set (%)
1	0.0776	0.0778	40.83	40.81
10	0.0574	0.0580	55.24	54.78
20	0.0420	0.0442	68.71	67.03
30	0.0322	0.0365	76.96	74.09
40	0.0250	0.0322	82.73	78.48
50	0.0188	0.0294	87.38	81.58
60	0.0142	0.0288	90.73	83.47
70	0.0108	0.0295	93.13	84.74
80	0.0085	0.0310	94.81	85.41

The traditional machine learning methods such as LSTM and CNN can achieve an accuracy of more than 80% in fault diagnosis; there is room for improvement in diagnosis accuracy. In recent years, transformers have been widely used to diagnose faults and achieve an excellent diagnostic effect. Based on the datasets, this study uses a Time Series Transformer (TST) [28] method to diagnose inter-shaft bearing faults. The TST model structure and parameters are shown in Fig. 23 and Table XI. The boxplot of loss function values and accuracies are shown in Fig. 24.

From the diagram of the model loss function of the test set in Fig. 24(c), the loss functions of the test set and test set

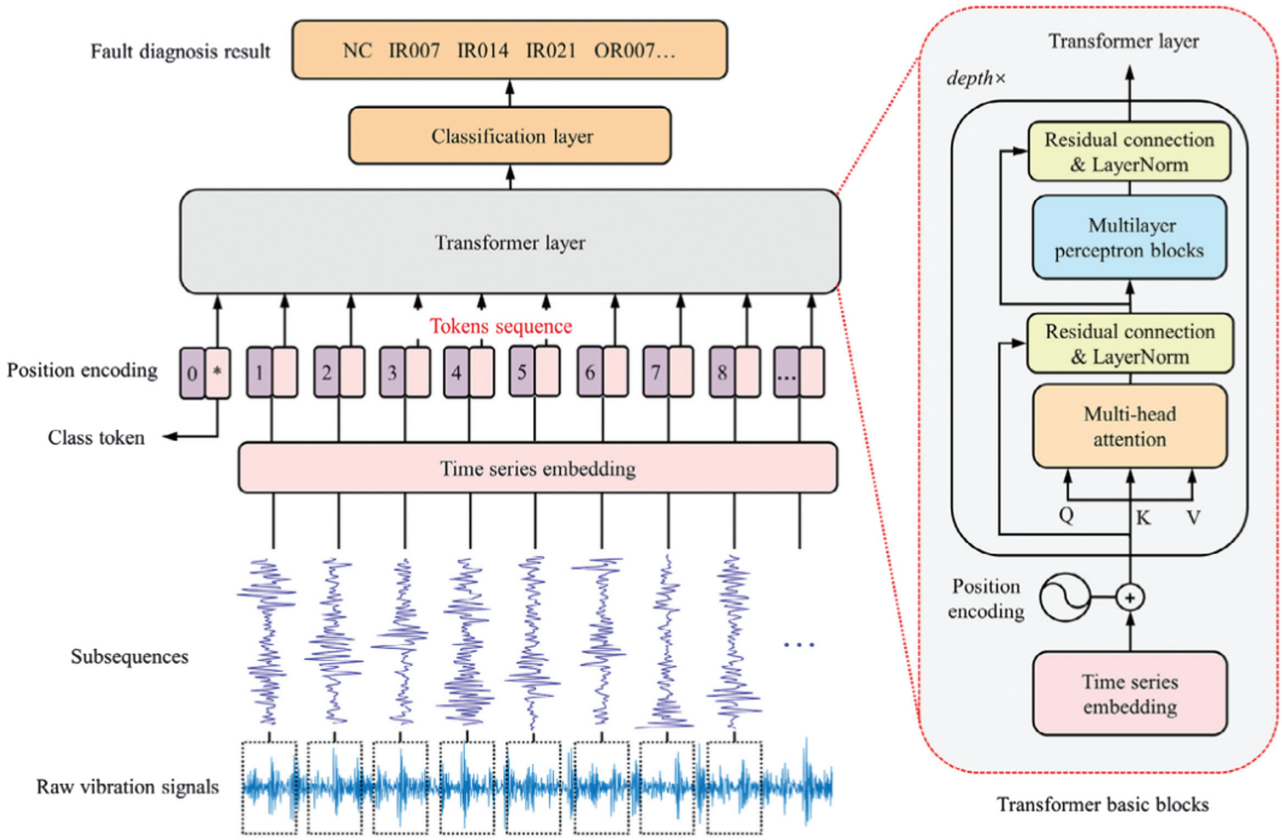

Fig. 23. Structure of TST model [28].

Table XI. The detailed structure of TST model

Model	Structure parameters							
	N_s	L/N_s	*dim*	dim_{MLP}	d_k	*h*	*depth*	Pos encoding
TST	256	8	128	256	64	8	4	1 D

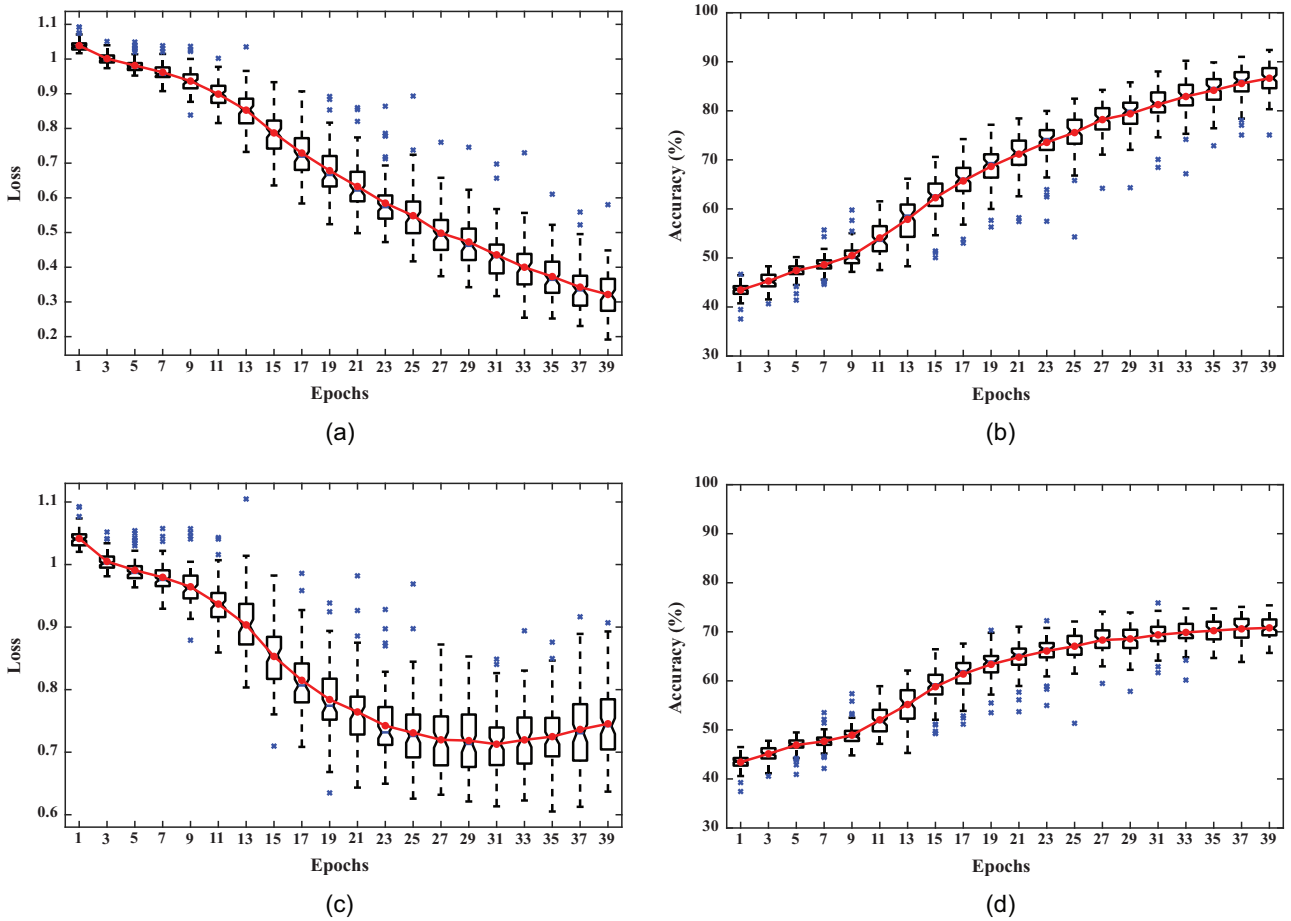

Fig. 24. The fault diagnosis results of TST. (a) Loss function value of training set. (b) Accuracy of training set. (c) Loss function value of test set. (d) Accuracy of test set.

decrease gradually with the increase of epochs and increases inversely after 30 epochs, which may also be the effect of dataset noise or TST structure. As is shown in Fig. 24, it can be seen that the test set accuracy receives a level of more than 80% over 30 epochs, and the test set accuracy is more than 70% at 35 epochs. It can be seen that TST does not show better diagnostic efficacy compared with CNN and LSTM, which deserves further study. The average loss function values and accuracies of the training set and test set are shown in Table XII.

Comparing the diagnosis results of this dataset with those based on other datasets in existing papers, the results are listed in Table XIII.

The results in Table XIII show that in the comparison of CNN, LSTM, and TST, the diagnosis accuracy of the dataset in this paper is lower than that of the existing bearing datasets. Compared with the accuracy of the dataset in this paper, the accuracy difference can reach a maximum of 40.40%. All these mean that the dataset in this paper is closer to the actual engineering and more difficult to

Table XII. The average loss function values and accuracies of TST

	Average loss function values		Average accuracy	
Epochs	Training set	Test set	Training set (%)	Test set (%)
1	1.0388	1.0416	43.45	43.43
5	0.9815	0.9909	47.43	46.91
10	0.0918	0.9510	52.04	50.23
15	0.7871	0.8531	62.28	58.80
20	0.6546	0.7753	70.08	64.26
25	0.5486	0.7309	75.56	67.06
30	0.4536	0.7199	80.36	69.08
35	0.3731	0.7249	84.18	70.24
40	0.3086	0.7480	87.19	71.07

Table XIII. Comparison of the diagnosis result based on dataset of this paper and others

	Accuracy				
Methodology	**Dataset of this paper (%)**	**CWRU (%)**	**Difference (%)**	**XJTU (%)**	**Difference (%)**
CNN	83.13	93.30	(−12.23)	98.00	(−17.89)
LSTM	85.41	92.07	(−7.80)	98.65	(−15.50)
TST	71.07	99.72	(−40.31)	99.78	(−40.40)

diagnose, which provides a new challenge for inspecting fault diagnosis methods.

V. CONCLUSIONS

This study built a test rig based on an aero-engine, which includes a motor drive system and a lubricant system. The vibration signals of the aero-engine under inter-shaft bearing faults were obtained by replacing the inter-shaft bearings with artificially faulty ones. The test data under different inter-shaft bearing conditions were integrated and processed to form a dataset of 2412 test data of aero-engine inter-shaft bearing faults. Based on this dataset, various methods, such as spectrum analysis, envelope spectrum analysis, CNN, LSTM, and TST, were used for fault diagnosis. The results showed that due to the difficulty of processing the signals of aero-engine housing, traditional fault diagnoses methods such as spectrum analysis and envelope spectrum analysis could not achieve effective fault diagnosis, while machine learning methods such as CNN, LSTM, and TST could achieve relatively effective fault diagnosis, but their performance is far inferior to that on existing datasets. Further study is needed to optimize the fault diagnosis method and make it more universal.

The future study can explore more effective fault diagnosis methods based on this dataset to verify the validity of the fault diagnosis methods, especially the improved methods based on the transformer. It can also develop research in aero-engine modal parameter identification and other aspects. Furthermore, the experiment in this study is based on motor drive, and combustion drive can be tested in the future which is closer to the actual aero-engine operating state. And the bearing cage and roller faults will be a good supplement to the dataset.

ACKNOWLEDGMENTS

The authors are very grateful for the financial supports from the National Natural Science Foundation of China (Grant No. 11972129), the Natural Science Foundation of Heilongjiang Province (Outstanding Youth Foundation, Grant No. YQ2022A008), and the Fundamental Research Funds for the Central Universities.

COMPETING INTERESTS

The authors declare that they have no conflict of interest.

DATA AVAILABILITY STATEMENTS

Data will be made available on request. The dataset of this paper is available at https://github.com/HouLeiHIT/HIT-dataset.

CONFLICT OF INTEREST STATEMENT

The authors declare no conflicts of interest.

REFERENCES

[1] JDMD Editorial Office, N. Gebraeel et al., "Prognostics and remaining useful life prediction of machinery: advances, opportunities and challenges," *J. Dyn. Monit. Diagn.*, vol. 2, pp. 1–12, 2023.

[2] H. Yi et al., "Nonlinear resonance characteristics of a dual-rotor system with a local defect on the inner ring of the inter-shaft bearing," *Chin. J. Aeronaut.*, vol. 34, pp. 110–124, 2021.

[3] S. Han and Z. Feng, "Deep residual joint transfer strategy for cross-condition fault diagnosis of rolling bearings," *J. Dyn. Monit. Diagn.*, vol. 2, pp. 51–60, 2023.

[4] L. Hou et al. "Feature extraction of weak bearing faults based on Laplace wavelet and orthogonal matching pursuit," *Shock Vib.*, vol. 2022, Art.ID. 8154492, 2022.

[5] R. Yang, Z. Zhang, and Y. Chen, "Analysis of vibration signals for a ball bearing-rotor system with raceway local defects and rotor eccentricity," *Mech. Mach. Theory*, vol. 169, Art.ID. 104594, 2022.

[6] J. Wang et al., "Improved spiking neural network for inter-shaft bearing fault diagnosis," *J. Manuf. Syst.*, vol. 65, pp. 208–219, 2022.

[7] M. Yu et al., "Compound faults feature extraction of inter-shaft bearing based on vibration signal of whole aero-engine," *J. Vib. Control*, vol. 29, pp. 51–64, 2023.

[8] X. Liu et al., "A combined deep learning model for damage size estimation of rolling bearing," *Int. J Engine Res.*, vol. 24, pp. 1362–1373, 2023.

[9] X. Liu et al., "Convolution neural network based particle filtering for remaining useful life prediction of rolling bearing," *Adv. Mech. Eng.*, vol. 14, pp. 1–15, 2022.

[10] W. Zhang et al., "Compound fault diagnosis of aero-engine rolling element bearing based on CCA blind extraction," *IEEE Access*, vol. 9, pp. 159873–159881, 2021.

[11] Z. Hou et al., "Siamese multiscale residual feature fusion network for aero-engine bearing fault diagnosis under small-sample condition," *Meas. Sci. Technol.*, vol. 34, Art.ID. 035109, 2023.

[12] X. Pan et al., "A study on the diagnosis of compound faults in rolling bearings based on ITD-SVD," *J. Vibroeng.*, vol. 23, pp. 587–602, 2021.

[13] H. Wang, J. Xu, and R. Yan, "Intelligent fault diagnosis for planetary gearbox using transferable deep Q network under variable conditions with small training data," *J. Dyn. Monit. Diagn.*, vol. 2, pp. 30–41, 2023.

[14] A. Smith and B. Randall, "Rolling element bearing diagnostics using the case Western Reserve University data: a benchmark study," *Mech. Syst. Signal Process.*, vol. 64–65, pp. 100–131, 2015.

[15] B. Wang et al., "A hybrid prognostics approach for estimating remaining useful life of rolling element bearings," *IEEE Trans. Reliab.*, vol. 69, pp. 401–412, 2020.

[16] D. Kumar et al., "Triaxial bearing vibration dataset of induction motor under varying load conditions," *Data Brief*, vol. 42, Art.ID. 08315, 2022.

[17] W. Jung et al., "Vibration, acoustic, temperature, and motor current dataset of rotating machine under varying operating conditions for fault diagnosis," *Data Brief*, vol. 48, Art.ID. 109049, 2023.

[18] C. Lessmeier et al., "Condition monitoring of bearing damage in electromechanical drive systems by using motor current signals of electric motors: a benchmark data set for data-driven classification," *Proc. Eur. Conf. Prognost. Health Manag. Soc.*, Bilbao, Spain, 2016.

[19] D. Verstraete et al., "Deep learning enabled fault diagnosis using time-frequency image analysis of rolling element bearings," *Shock Vib.*, vol. 2017, pp. 1–17, 2017.

[20] M. Bin, "Current based condition monitoring of electromechanical systems. Model-free drive system current monitoring: faults detection and diagnosis through statistical features extraction and support vector machines classification," University of Bradford, 2013.

[21] S. Porotsky, "Remaining useful life estimation for systems with non-trendability behavior," in *IEEE Conf. Prognost. Health Manag. (PHM- 2012)*, Beijing, China, 2012.

[22] S. Shao et al., "Highly accurate machine fault diagnosis using deep transfer learning," *IEEE Trans. Ind. Inf.*, vol. 15, pp. 2446–2455, 2019.

[23] P. Nectoux et al., "PRONOSTIA: an experimental platform for bearings accelerated degradation tests," in *IEEE Int. Conf. Prognost. Health Manag. (PHM- 2012)*, Beijing, China, 2012.

[24] E. Sutrisno et al., "Estimation of remaining useful life of ball bearings using data driven methodologies," in *IEEE Conf. Prognost. Health Manag. (PHM- 2012)*, Beijing, China, 2012.

[25] W. Gousseau et al., "Analysis of the rolling element bearing data set of the center for intelligent maintenance systems of the University of Cincinnati: CM2016," in *13th Int. Conf. Cond. Monit. Machin. Fail. Prev. Technol.*, Paris, France, 2016. pp. 1–13.

[26] H. Qiu et al., "Wavelet filter-based weak signature detection method and its application on rolling element bearing prognostics," *J. Sound Vib.*, vol. 289, pp. 1066–1090, 2006.

[27] P. Cao, S. Zhang, and J. Tang, "Preprocessing-free gear fault diagnosis using small datasets with deep convolutional neural network-based transfer learning," *IEEE Access*, vol. 6, pp. 26241–26253, 2018.

[28] Y. Jin, L. Hou, and Y. Chen, "A time series transformer based method for the rotating machinery fault diagnosis," *Neurocomputing*, vol. 494, pp. 379–395, 2022.